Internal Temperature Estimation for Lithium-ion Batteries Through Distributed Equivalent Circuit Network Model

Li, S., Patel, A., Zhang, C., Amietszajew, T., Kirkaldy, N., Offer, G. J. & Marinescu, M

Published PDF deposited in Coventry University's Repository

Original citation:
Li, S, Patel, A, Zhang, C, Amietszajew, T, Kirkaldy, N, Offer, GJ & Marinescu, M 2024, 'Internal Temperature Estimation for Lithium-ion Batteries Through Distributed Equivalent Circuit Network Model', Journal of Power Sources, vol. 611, 234701.
https://doi.org/10.1016/j.jpowsour.2024.234701

DOI 10.1016/j.jpowsour.2024.234701
ISSN 0378-7753
ESSN 1873-2755

Publisher: Elsevier

© 2024 The Authors. Published by Elsevier B.V. This is an open access article under the CC BY license (http://creativecommons.org/licenses/by/4.0/).

Journal of Power Sources 611 (2024) 234701

Contents lists available at ScienceDirect

Journal of Power Sources

journal homepage: www.elsevier.com/locate/jpowsour

Internal temperature estimation for lithium-ion batteries through distributed equivalent circuit network model

Shen Li [a,c,1], Anisha N. Patel [a], Cheng Zhang [b], Tazdin Amietszajew [b], Niall Kirkaldy [a,c], Gregory J. Offer [a,c], Monica Marinescu [a,c,*]

[a] Department of Mechanical Engineering, Imperial College London, London, SW7 2AZ, United Kingdom
[b] Institute for Clean Growth & Future Mobility, Coventry University, Coventry, CV1 5FB, United Kingdom
[c] The Faraday Institution, Harwell Science and Innovation Campus, Didcot, OX11 0RA, United Kingdom

HIGHLIGHTS

- Developed 3D distributed electro-thermal model for internal temperature estimation.
- Model parameterized and validated experimentally for 21700 cylindrical cells LGM50T.
- Direct core temperature is used for validation of internal cell temperature.
- Estimation of core temperature based on surface temperature measurement succeeds.
- Prior methods are inaccurate at high discharge due to high internal thermal gradients.

ARTICLE INFO

Keywords:
Lithium-ion battery
Internal temperature estimation
Kalman filter
Electro-thermal model

ABSTRACT

Lithium-ion cells experience significant internal thermal gradients during operation, with a direct impact on their safety, performance, cost and lifetime. The estimation of the internal temperature of cells is therefore particularly important. In this work, a 3D distributed electro-thermal model for internal temperature estimation is developed for a cylindrical cell (LG M50T, NMC811). The model is parameterized and comprehensively validated against experimental data for 21700 cells, including direct core temperature measurements. Multiple types of electrical load are considered, including constant current discharge, pulse discharge, drive cycle and instant discharge/charge switching. The developed model is used to estimate core temperature based on surface temperature measurement. The predictions are shown to have good accuracy at relatively low computational cost. We show that the widely adopted two-node lumped thermal estimation model is increasingly inaccurate for more aggressive discharges, when thermal gradients become higher. Compared to the standard two-node model, the distributed equivalent circuit network model predicts the effects of detailed internal cell structure (electrode, current collector, metal can and tab) and distributed internal heat generation. The results are of immediate interest to cell manufacturers and battery pack designers, while the modelling and parameterization framework is a useful tool for energy storage systems design.

1. Introduction

Energy storage technologies have a significant contribution to reaching the global Net-zero emission target [1]. Lithium-ion batteries (LIBs) are among the most popular energy storage solutions for mobility, power tools and personal devices due to their energy and power densities. To further reduce both the economic and environmental costs associated with LIBs, there is a strong need to improve the efficiency and electrical/thermal performance of LIBs.

The temperature profile inside cells has a direct effect on the discharge capacity performance and battery lifetime for electric vehicle (EV) and battery energy storage system (BESS) industry [2–6]. Battery safety issues such as thermal runaway can be caused by high internal temperatures [7] or penetration [8]. The internal temperature can also

* Corresponding author. Department of Mechanical Engineering, Imperial College London, London, SW7 2AZ, United Kingdom.
E-mail address: monica.marinescu@imperial.ac.uk (M. Marinescu).
1 Present address: Rimac Technology R&D UK Limited, Wellesbourne Campus, Warwick CV35 9EF, United Kingdom.

https://doi.org/10.1016/j.jpowsour.2024.234701
Received 20 July 2023; Received in revised form 30 April 2024; Accepted 7 May 2024
Available online 25 May 2024
0378-7753/© 2024 The Authors. Published by Elsevier B.V. This is an open access article under the CC BY license (http://creativecommons.org/licenses/by/4.0/).

be an indicator in early detection of internal short circuits [9]. Thermal gradients are easily generated inside LIB and the temperature inhomogeneity can be detrimental to battery health. Experimental studies have shown that the thermal gradient inside a pouch cell can accelerate the degradation by 3 times [10]. In comparison to pouch cells, cylindrical cells have a poorer ability to dissipate heat, making thermal gradients more probable [11]. Under galvanostatic impedance spectroscopy with 10C peak to peak current (30C maximum rated discharge current for the particular cell used) and convection boundary conditions, the temperature difference across the cell surface can become higher than 5 °C [12]. This indicates that the core of the cell could be at significantly different temperatures than a point on the cell surface, and that there may be significant temperature gradients within the jellyroll. Therefore, estimating internal temperature in real-time during operation adds significant value to improving performance, lifetime and safety in battery systems.

Surface temperature can be directly measured relatively easily, however, it is far less practical to insert a temperature sensor inside a cell for commercial purposes. Although an in-cell thermocouple technique [13] has proven useful for research purposes, it is still not suitable for massive battery production, due to chemical stability of the thermocouple and the added cost. Distributed thermal models have been developed to simulate and predict the battery's internal temperature distribution, but this prognostic method type suffers from error accumulation, especially during long-time simulation. Data-driven method has proven successful for battery internal temperature estimation with high accuracy [14], however, its significant drawback is the extremely large amount of training data required.

The virtual thermal sensor (VTS) method has proven useful in detecting the real-time internal temperature [15–18]. Variations of Kalman Filters (KF) were implemented within the thermal model to perform internal temperature estimation. There are majorly three categories of VTS temperature estimation methods, differentiated by the type of model they are based on: two/three-node thermal model, reduced-order model and fundamental continuum model. The two-node model for cylindrical cell [16] and prismatic cell [17] were proposed for internal temperature estimation. Only two nodes are placed along the electrode thickness direction. These two-node thermal models have low computational cost but limited accuracy, so that the C rate is restricted to below 1C, if the model predictions are to be trusted. The accuracy of the two-node thermal model was improved by considering electrical-thermal coupling [15,18], but still the models were limited to mild electrical loads only. In the second VTS category, the reduced-order thermal model has proven effective in the estimation of volume-averaged temperature and temperature differences within the cell [19]. Core temperature can be estimated based on straightforward impedance measurement [20]. However, these efficient reduced-order modelling approaches are limited to mild discharge current conditions and 2D simplification. The latter constraint renders these methods unsuitable for realistic, application-relevant thermal boundary conditions, such as side and bottom cooling. In the third VTS category, temperature estimation is performed on physics-based continuum models [21]. The bulk cell average temperature is successfully estimated by applying Extended Kalman Filter (EKF) on a lumped electrochemical-thermal model [21]. However, such continuum models are not suitable for spatially-distributed temperature estimation due to their relatively high computational cost [17]. Until now, there has been a lack of tools for efficient estimation of the internal temperature distribution under a wide range of electrical loads and application-relevant thermal boundary conditions.

Here we introduce an innovative internal temperature estimation tool with practical computational cost and accuracy, valid under a wide range of electrical loads for application: e.g., under the aggressive 2C constant current discharge, the core temperature and voltage are estimated with a root-mean-square error (RMSE) of 0.89 °C and 11.13 mV. The efficiency of the tool is enabled by inheriting the efficiency properties from the improved equivalent circuit network (ECN) framework [22]. The equivalent circuit network (ECN) [23–26] was widely used for modelling internal temperature gradients owing to its relative ease of parametrization and low computational cost. Recently, the improved ECN framework [22] was created for cylindrical cells and has proven effective in capturing flexible thermal boundary conditions and thermal effects due its detailed account of the cell's internal structure (tab location, jellyroll, metal can, etc.). In the current work, an internal temperature estimation tool using the ECN framework is proposed and validated against experimental data from instrumented cylindrical cells with inserted thermocouples.

The rest of the paper is organized as follows: Section 2 presents the internal temperature estimation model. Section 3 describes the in-cell thermocouple instrumentation and experimental setup for model parametrization and model validation. Section 4 presents the validation of thermal estimation under a wide range of application scenarios, including constant current discharge, pulse discharge, drive cycle and discharge/charge instant switching. The established estimation model is compared with a conventional two-node thermal estimation model.

2. Model description

2.1. Distributed Equivalent Circuit Network (dECN) model

The cell-level distributed model is composed of coupled electrical and thermal domains and is implemented using an ECN framework [22]. Given the initial conditions and boundary conditions, it creates a temporal and spatial description of various quantities of interest such as the current density and temperature within the cylindrical cell geometry.

Fig. 1(a) shows a schematic description of the dECN model for cylindrical cell. A cylindrical jellyroll consisting of interleaved realistic arrangements of electrodes and separators forms the computational domain, and is encapsulated by elements representing the thermal properties of the metal can. The connections to the external current-conducting tabs are also included. It was found that the jellyroll core area is mostly filled with separator for LG M50T cell [22], which is reflected by the core area elements in the model. The geometry of the computational domain is such that the angular direction of the jellyroll corresponds to the x axis in the proposed co-ordinate system and is represented by the Archimedes spiral equation. The axial and radial directions of the jellyroll correspond to the y and z axes, respectively. The computational domain is discretized into multiple elements, wherein within each element, all the constituent components (anodes, cathodes, separators and the two current collectors) are arranged in a stacked configuration. Each distributed element is described by an elementary ECN, which captures the electrical and thermal behavior within that element. The coupling between the electrical and thermal model is as follows: for current collectors, the irreversible heat generation caused by their electrical resistance contributes to the heat source in the thermal model; for electrodes, both irreversible heat generation by electrical resistance and reversible heat generation by entropy contribute to the heat source.

The fundamental heat transfer equations [27] are modified for the electrode, separator and current collector materials given by:

$$\rho c\frac{\partial T}{\partial t}=\nabla\cdot(\lambda\nabla T)+q=\lambda_x\frac{\partial^2 T}{\partial x^2}+\lambda_y\frac{\partial^2 T}{\partial y^2}+\lambda_z\frac{\partial^2 T}{\partial z^2}+q, \tag{1}$$

where ρ, c, λ are the specific mass density, specific heat capacity, heat transfer coefficient with values for all materials given in Table I. T is the temperature of the material. λ_x, λ_y and λ_z are the heat transfer coefficients in the three directions, and q is the heat source.

The finite difference method is adopted to discretize the heat transfer equation i.e., Eq. (1). The discretized equation under the Crank-Nicolson (CN) method is given by:

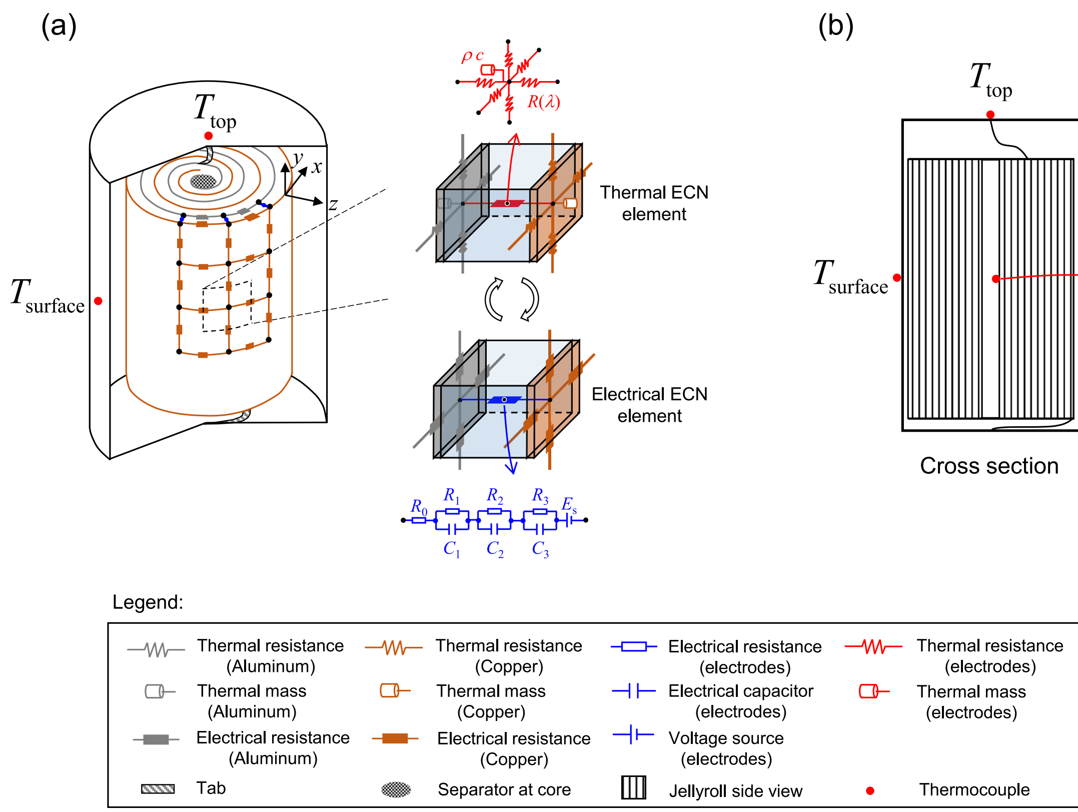

Fig. 1. Schematic representation of the cell-level model. (a) Cylindrical cell geometry containing jellyroll, tab and can. The electrical/thermal model element containing electrode and current collector components is magnified. (b) Cross section representation of the internal structure of the cylindrical cell. The temperature locations for core temperature T_{core}, side surface temperature $T_{surface}$ and positive tab temperature T_{top} are indicated.

Table 1
Thickness and thermal properties of cell components [23,28].

Component	Thickness (μm)	Thermal conductivity λ (W·m^{-1}·K^{-1})	Heat capacity c (J·kg^{-1}·K^{-1})	Mass density ρ (kg·m^{-3})
Aluminum foil	16.33	238.00	903.00	2702.00
Copper foil	27.00	398.00	385.00	8933.00
Anode	86.15	1.58	1437.00	1555.00
Cathode	77.03	1.04	1270.00	2895.00
Separator	14.00	0.34	1978.00	1017.00
Can	160.00	238.00	903.00	2702.00

$$A \cdot T_k = B \cdot T_{k-1} + u_{k-1}, \tag{2}$$

where T_k is the calculated temperature for each node at time step k and T_{k-1} is the node temperature calculated at the last time step. u_{k-1} is the vector containing the heat generated within one time-step. A and B are the thermal conductivity matrices generated by the finite difference discretization in implicit CN method.

In the model presented here, a distributed model of 1020 electrical/thermal ECN elements is used. The number of elements is decided by the minimum value that still passes the convergence check. The elements are distributed in configuration of 4 elements along the angular direction (x axis), 15 elements along axial direction (y axis) and 19 elements (1 for the hollow separator area, 17 for the electrodes and 1 for the metal can) along the radial direction (z axis), as shown in Fig. 1(a).

The dECN model assumptions are listed below. For the electrical model, the voltage response is represented by an equivalent circuit model of one series resistance and three RC pairs for each ECN element. For the thermal model, the heat transfer processes inside the jellyroll and between jellyroll and metal can are assumed to follow Fourier's law. Perfect interfacial thermal connection between current collector and electrodes is assumed. Advection and radiation heat transfer are ignored.

In comparison to the fundamental battery modelling approaches [29,30], dECN is an empirical model that captures the voltage, current and heat generation with 3D spatial resolution. The high accuracy of the ECN model for the same cell (LG M50T) has been confirmed in our previous work [22]. The dECN model does not directly model the complex electrochemical processes such as lithium diffusion, charge transfer and chemical reactions. Therefore, dECN is a lightweight model suitable for real-time core temperature estimation. The model, however, can be easily modified to reflect other cylindrical cell geometries and other cell form factors, e.g., the dECN model was modified for a 4680 tabless cell [31], and validated for a pouch cell [32] and a prismatic cell [33].

2.2. Kalman Filter for temperature estimation

The temperature estimation was performed by the implementation of a Kalman Filter (KF) algorithm [34] for internal temperature estimation in conjunction with the dECN model described in Section 2.1, for which the thermal model is converted to state-space representation. The temperatures of all nodes are chosen as the states to be estimated. In the process model, the predicted state estimate $\hat{x}_k$ is given as:

$$\hat{x}_k = Fx_{k-1} + u_{k-1} + w_{k-1}, \tag{3}$$

where F is the state transition matrix. Following Eq. (2), the state transition matrix here is calculated as:

$$F = A^{-1}B. \tag{4}$$

x_{k-1} is the previous state vector, here the given temperature of all nodes at the previous time step, i.e., $x_{k-1} = \left[T^1, T^2, \dots T^N\right]_{k-1}^T$. u_{k-1} is the control vector, which contains the heat generation and applied thermal boundary condition. w_{k-1} is the applied process noise vector that is assumed to follow zero-mean Gaussian distribution with covariance Q.

For the measurement model, the relationship between the state and measurement is given as:

$$z_k = Hx_k + \nu_k, \tag{5}$$

where z_k is the measurement vector. For example, in Fig. 1(b)–if the internal temperature T_{core} in the cell core and the side surface temperature $T_{surface}$ are measured in the experiments, then the measurement vector is $z_k = \left[T_{core}, T_{surface}\right]^T$. H is the measurement matrix and is calculated as:

$$H = \frac{\partial z_k}{\partial x_k}. \tag{6}$$

ν_k is the measurement temperature noise that is assumed to follow zero-mean Gaussian distribution with covariance R.

The prediction and update procedures are described as follows. The predicted error covariance P_k for the new time step is given as:

$$P_k = FP_{k-1}F^T + Q. \tag{7}$$

The measurement residual y_k at the new time step k is the difference between the measurement value and the predicted value:

$$y_k = z_k - H\widehat{x}_k. \tag{8}$$

The Kalman gain K_k at the new time step is calculated by the predicted error covariance P_k and measurement matrix H as:

$$K_k = P_kH^T\left(R + HP_kH^T\right)^{-1}. \tag{9}$$

With the KF gain and predicted value, the estimated state (corrected temperature) is updated as:

$$\widehat{x}_k = \widehat{x}_k + K_ky_k. \tag{10}$$

Finally the error covariance is updated by:

$$P_k = (I - K_kH)P_{k-1}. \tag{11}$$

3. Experimental

Experiments were performed on LG M50T (LG INR21700-M50T) cylindrical lithium-ion cells. These cells utilise a SiO_x-doped graphite negative electrode alongside a $LiNi_{0.8}Mn_{0.1}Co_{0.1}O_2$ (NMC 811) positive electrode, with a nominal capacity of 18.2 Wh (5 Ah). Cells were stored at 10 °C when not in use. All electrochemical experiments were performed on 3 separate cells simultaneously under the same conditions.

3.1. Cell instrumentation with in-cell thermocouple

Internal cell temperature measurements were made possible by inserting K-type thermocouples into the cell core. The thermocouples were coated in micron-thin conformal layer of chemically neutral polymer prior to insertion, to prevent corrosion and to avoid interference with the cell chemistry. The measurements obtained are representative of the temperature at the central axis mid-height of the jellyroll. Measurements were also taken by thermocouples attached to the surface of the cell, as shown in Fig. 2.

Before instrumentation, fresh cells were discharged to their minimum operating voltage and transferred to an argon-filled glovebox with O_2 and H_20 traces below 1 ppm. The cells were opened at the positive/cathode cap. Any interference with the cell structure can affect the cell performance. To avoid this, the thermocouple was located in the space in the core of the cell, a space free of electrodes and current collectors left by the manufacturing process of creating the jellyroll. The instrumentation methodology was designed in such a way so as to least interfere with the current path (i.e. current collectors, tabs, weld point and connector points), as schematically shown in Fig. 2(a). The cells were re-sealed after sensor insertion. The impact of this cell modification on the cell performance has been evaluated previously and found negligible [35]. More details on the cell modification procedure are available in Fleming et al. [35] and Li et al. [22].

Fig. 2(b) shows an example of a modified cell used in this study. The electrochemical performance of the instrumented cells was compared to that of the fresh cell for a 0.3C constant current discharge at 25 °C in a thermal chamber. The corresponding terminal voltages of the three modified cells and the unaltered cell are shown in Fig. 2(c). The capacity of the modified cell appears slightly higher than that of the unaltered cell, possibly due to degassing [36].

3.2. Parametrization of the electrical network model

The experimental data used for model parameterization/validation in this study was limited to discharge loads. Prior to any discharge experiment, the cells were first charged to 100 % SoC using the standard charging procedure outlined in the cell specification sheet. This consisted of a constant current (CC) charge at a C-rate (current divided by nominal capacity) of 0.3C (1.5 A) until the upper voltage limit of 4.2 V was reached, with a subsequent constant voltage (CV) charge at 4.2 V until the current dropped below 0.01C (50 mA). This standard charge was always performed at a temperature of 25 °C in a thermal chamber for both parameterization tests here and validation tests in the next section. The cell was then rested for 2 h at 25 °C under open circuit conditions to allow the open circuit voltage (OCV) to equilibrate. We used this starting point to define 100 % SoC for subsequent discharge experiments, thus ensuring a consistent starting point between tests.

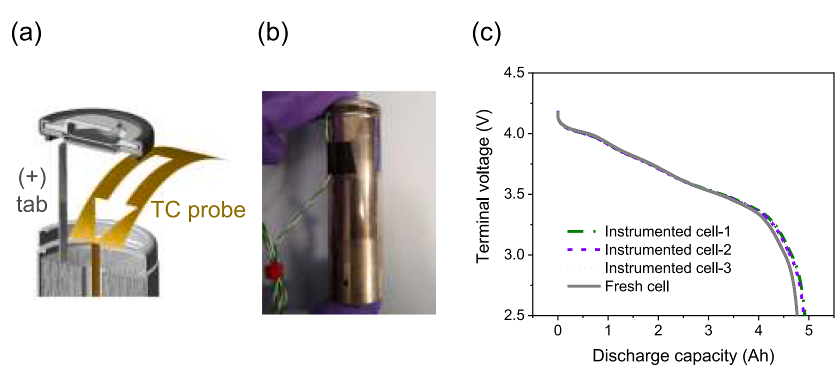

Fig. 2. In-cell thermocouple instrumentation. (a) Schematic concept of the sensor insertion (Reproduced from Ref. [22]). (b) Cylindrical LG M50T cell with inserted thermal probe for core temperature monitoring. (c) Terminal voltage during a 0.3C constant current discharge at 25 °C in a thermal chamber.

After performing this standard charge at 25 °C, the temperature of the thermal chamber was adjusted to the set-point required for the subsequent discharge experiment, and the cell was held under open circuit conditions until thermal equilibrium under the new ambient temperature was reached.

The values for the circuit components of the electrical model (resistances and capacitances) are formulated as lookup tables. They are obtained via the experimental parameterization procedure described in this section, from pulse discharge tests. All the test data used for model parameterization is shown in the Supplementary material A, along with the details of the parameter identification procedure and mathematical equations used.

From pseudo-OCV data for this cell recorded at a discharge current of 0.01C at 25 °C, a voltage vs SoC curve was produced. This data was then used to tailor a set of pulsed discharge, i.e., Galvanostatic Intermittent Titration Technique (GITT) experiment for this specific cell. Varying the charge passed in each current pulse enabled a high density of data points (every 1 % SoC) in areas of high rapid change of the pseudo-OCV vs SoC curve, and a lower density of points (every 4–6% SoC) in areas where a relatively linear relationship between pseudo-OCV and SoC was observed. This approach optimized the resolution of data points across the SoC range, whilst keeping the test duration manageable. The current during discharge pulses was 1C (5 A). The low voltage cut-off was 2.5 V as specified in the cell datasheet. Due to the slower relaxation of the cell at lower SoC values, the rest periods between current pulses were extended for the lower SoC regions. This pulsed-current experiment was performed at 5 different temperatures (15 °C, 25 °C, 35 °C, 45 °C, and 55 °C) in a thermal chamber.

In addition to the 1C pulse test, the batteries were also tested using 2C pulses, starting from 100 % SoC until end of discharge, defined by the cell reaching 2.5 V. A rest period of 1 h was used between pulses. Two tests were conducted, each with a different pulse width, i.e., corresponding to 4 % SoC and 20 % SoC. These 2C pulse tests were repeated at 3 different temperatures (25 °C, 35 °C, and 45 °C) in a thermal chamber.

Further, the batteries were also tested under CC discharge at 1C and 2C, from 100 % SoC until the terminal voltage reached 2.5 V. These CC tests were conducted at 3 different temperatures (25 °C, 35 °C, and 45 °C) in a Binder thermal chamber.

The novel features of the proposed parameter identification algorithm are summarized as follows. First, both pulse discharge tests and CC discharge test data were used for identifying the values of the electrical circuit components, which increases model accuracy under a wide range of load conditions [37]. Second, the nonlinear and linear model parameters are optimized separately. This reduces the optimization complexity and ensures the global optimum of the linear parameters. Third, all the resistor parameters for the full SoC operating range and the 5 temperature levels and 2 C-rate levels (i.e., 1C and 2C) are simultaneously identified, and constraints imposed on parameter values are used to ensure their smooth transitions across the full temperature range, i.e., the resistance value increases smoothly as the temperature drops. The Root Mean Square Error (RMSE) of the parameterization is 11.7 mV over the whole GITT parametrization process.

3.3. Cell validation testing

Instrumented cells were tested in a Binder thermal chamber that maintains the ambient air at the set temperature of 25 °C. Cells were electrically connected by welding nickel tabs to the positive and negative terminals then clamping the tabs down to a Perspex plate using brass busbars to which current and sense pins can be inserted. Seven K-type thermocouples were used to measure the temperature gradients with accuracy of ca. ±0.5 °C by positioning them as shown in Fig. 3 using Kapton tape. One K-type thermocouple was positioned above the cells to measure the ambient air temperature. Temperature measurements were recorded using a Pico TC-08 data logger (sampling frequency of 0.2 Hz). Measurements from the in-cell thermocouple was recorded by the Biologic (BCS-815) battery tester and used as a safety control.

Each set of experiments was carried out on three instrumented cells. Preconditioning tests were also carried out on one unmodified cell from the same manufacturing batch as the instrumented cells for a performance check.

Tests were initiated with preconditioning cycles by charging and discharging under constant current, constant voltage (CC-CV) control at a C-rate of 0.2C between the voltage limits of 4.2 V and 2.5 V. Cells then underwent a series of validation tests as detailed below. The following load scenarios were performed:

- Constant current discharge tests at both 1C and 2C until the lower voltage limit was reached.
- Pulsed discharge tests were performed at 2C, with 5 current pulses each passing 1000 mA h of charge until the lower voltage limit was reached. The cell was rested for 1 h between each pulse.
- A drive cycle based on the Worldwide Harmonised Light Vehicle Test Procedure (WLTP) [38] was applied to the cells. This procedure was scaled into a C-rate vs time profile with a maximum charging C-rate of 0.5C. The procedure was repeated until the lower voltage limit of 2.5 V was reached.
- Discharge/charge switching condition. Finally, discharge-charge swapping tests at 1C were performed. The cell was discharged from 100 % SoC down to 10 % SoC, charged up to 90 % SoC, discharged down to 10 % SoC, and finally charged up to near 30 % SoC. There is no rest during the test. The voltage limits (as stated above) as well as Coulomb counted capacity limits on discharge (initial >4500

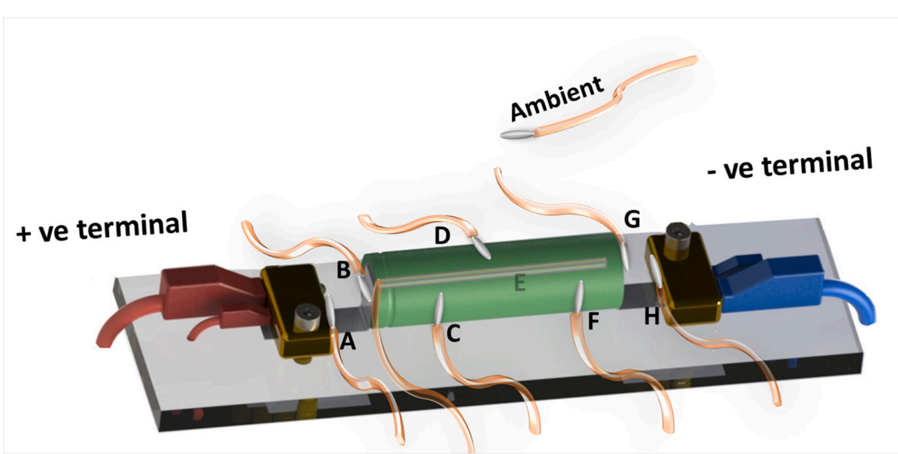

Fig. 3. Schematic of the experimental setup.

mA h, subsequent cycles >4000 mA h) and each charge step (<4000 mA h) were applied as additional criteria for ending the charge and discharge.

4. Results and discussion

4.1. Model validation

The distributed electro-thermal model was validated against different discharge/charge scenarios: constant current discharge, drive cycle, pulse discharge and current switching. These scenarios were designed to cover a wide range of the working conditions for the cell in the engineering application. For those validation experiments, the instrumented cell with internal thermocouple was used. In the simulation setup, convective boundary condition of $h = 30\ W/(m^2K)$ (typical values range in-between $0 - 60\ W/(m^2K)$ under forced air convection condition [27]) is applied on side surface with the ambient temperature of 25 °C. The positive and negative tab (top and base of the cell) temperature is set as Dirichlet boundary condition, i.e., the experimentally measured temperature at welding nickel tabs (position B and G in Fig. 3) is set as the temperature in the model. Here the tab temperature measurement is used only for the purpose of correction, to account for the small heat loss through welding nickel tabs. The tab temperature measurement is not necessary in real application when heat loss through the cell connection is mostly negligible.

4.1.1. Constant current discharges

The 1C (5 A) and 2C (10 A) currents were used for the constant current discharge scenarios. The 2C discharge corresponds to the maximum C rate allowed according to the specification sheet of the LG M50T cell, and thus forms an extreme condition test while within permissible boundaries of operation. Fig. 4(a, c and e) show model predictions and experimental results for the 1C discharge. In Fig. 4(a), during the 1C discharge process, the simulated terminal voltage (orange dotted curve) matches the experimental results (grey solid curve) with an RMSE of 14.32 mV. The cell SoC (blue dash-dotted curve) decreases

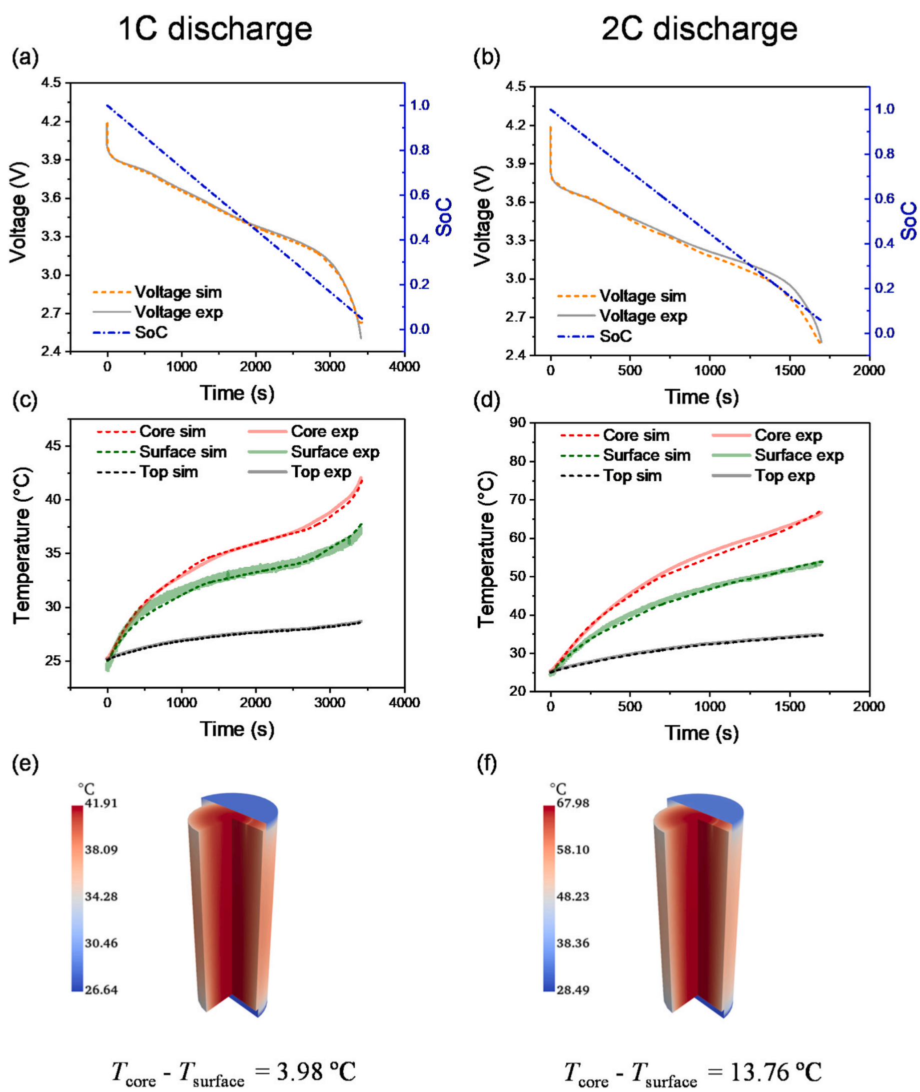

Fig. 4. Model validation: experimental and simulation results for 1C and 2C constant current discharges. Terminal voltage and corresponding SoC (as calculated by Coulomb counting) for (a) 1C and (b) 2C discharge. Temperature at different locations within the cell: core, side surface at middle height and positive tab for (c) 1C and (d) 2C discharge. Model-predicted temperature distribution throughout the cell at the end of the (e) 1C and (f) 2C discharge. The experimental tests were repeated twice on two instrumented cells and the experimental measurements are highly reproducible. For visual simplicity, only the first test result is shown in (a–d). The difference between experimental measurements and simulation is RMSE of 7.73 mV, 0.66 °C and 0.3 °C for the terminal voltage, core and surface temperature of 1C discharge in (a) and (c), RMSE of 11.13 mV, 0.89 °C and 0.66 °C for the terminal voltage, core and surface temperature of 2C discharge in (b) and (d).

from 100 % down to close to 0 % (Coulomb counted) as the cut-off voltage of 2.5 V is reached earlier than 0 % SoC. Fig. 4(c) shows the model-predicted core temperature (red dotted curve) and the experimentally measured internal temperature (red solid curve), as detected by the in-cell thermocouple. The simulated surface temperature (green dotted curve) and measured surface temperature (green solid curve) are shown in Fig. 4(c). The measured positive tab temperature (black solid curve) is set as the known temperature boundary condition in the simulation (black dotted curve), and thus the model predictions are overlapping with the data in Fig. 4(c). It is seen that the modelling results closely track the measured values for both core and surface temperatures. The RMSEs between the predicted and the experimentally measured values are 0.25 °C and 0.35 °C for core temperature and surface temperature, respectively. Fig. 4(e) shows the predicted temperature distribution at the end of discharge. The internal thermal gradient is significant in this 1C discharge process, as the temperature difference between the core and the surface reaches 4 °C at the end of discharge. Temperature differences of this magnitude were experimentally shown to significantly accelerate the rate of degradation a cycling test [10].

Fig. 4(b, d and f) show model predictions and experimental results for the 2C discharge. In Fig. 4(b) the model-predicted terminal voltage matches the measured value with an RMSE of 48.13 mV. As shown in Fig. 4(d), the measured core temperature (red dotted curve) is predicted by the simulated core temperature (red solid curve) with an RMSE of 0.79 °C. The measured surface temperature (green dotted curve) is also close to the simulated surface temperature (green solid curve) with an RMSE of 0.58 °C. The model-predicted internal temperature distribution is shown in Fig. 4(f). The temperature difference between the core and surface reaches 13 °C. The large thermal gradient along the radial direction of the cell can be explained by considering the equivalent thermal conductivities of the cell in the radial vs the axial directions: 1.17 W $m^{-1}K^{-1}$ (along radial direction) vs. 37.91 W $m^{-1}K^{-1}$ (along axial direction), as calculated in the previous work [22].

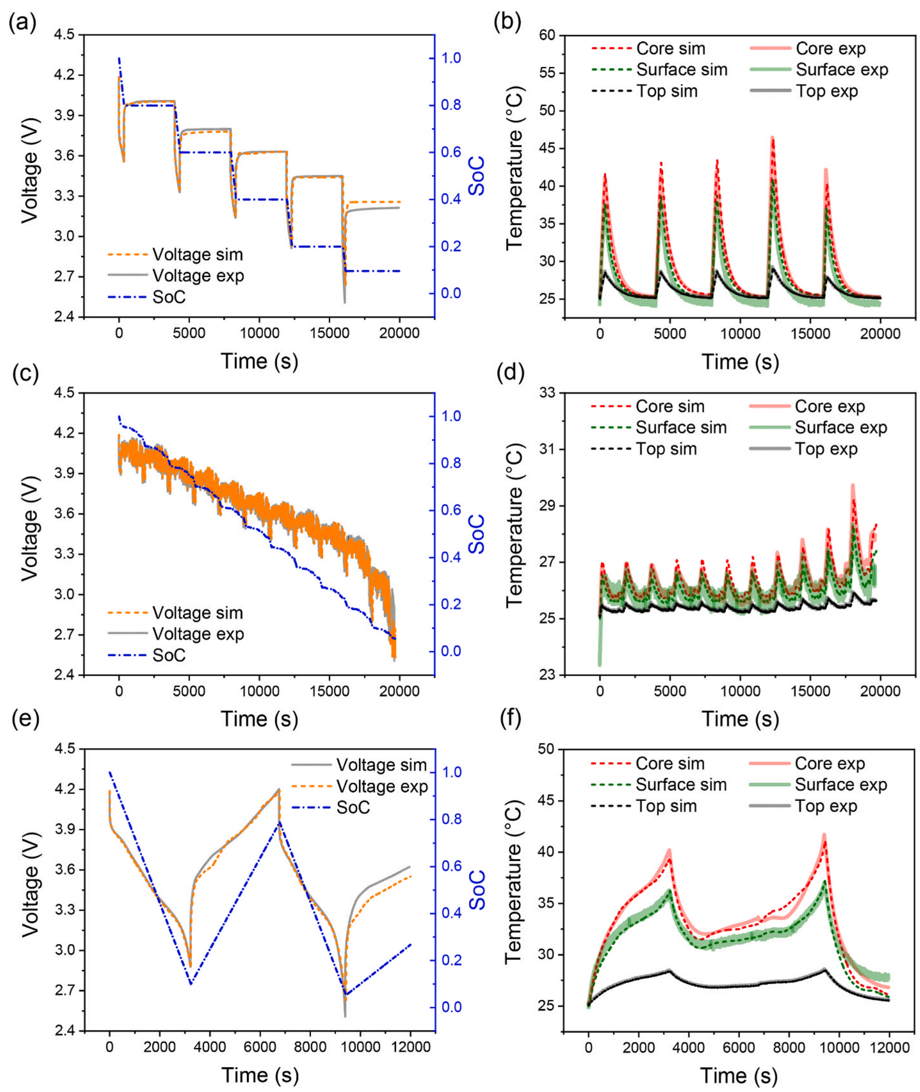

Fig. 5. Model validation: experimental and simulation results for different current profiles: pulse discharge, drive cycle and current-switching. (a) Terminal voltage and (b) temperature for pulse discharge at 2C. (c) Terminal voltage and (d) temperature for drive cycle load. (e) Terminal voltage and (f) temperature for discharge-charge current switching load. The experimental tests were repeated twice on two instrumented cells and the experimental measurements are highly reproducible. For visual simplicity, only the first test result is shown in (a–f). The difference between experimental measurements and simulation is RMSE of 8.30 mV, 0.57 °C and 0.51 °C for the terminal voltage, core and surface temperature of pulse discharge in (a) and (b), RMSE of 1.93 mV, 0.45 °C and 1.20 °C for the terminal voltage, core and surface temperature of drive cycle load in (c) and (d), RMSE of 18.53 mV, 0.72 °C and 0.39 °C for the terminal voltage, core and surface temperature of drive cycle load in (e) and (f).

4.1.2. Pulse discharge

In the pulse discharge experimental test, the cell was discharged at 2C from 100 % SoC to 0 % SoC in 5 discharge/relaxation periods. As shown in Fig. 5(a), the model-predicted terminal voltage matches the experimental results with an RMSE of 28.60 mV. The thermal gradient, taken as the difference between the experimentally measured core and surface temperatures reaches its highest value (approximately 2.5 °C) at the end of each discharge pulse, as seen in Fig. 5(b). The model-predicted temperature agrees with the experimental results with RMSE of 0.52 °C and 0.99 °C for core and surface temperatures, respectively.

4.1.3. Drive cycle

The drive cycle scenario resembles more closely common practical use of a cell, compared to full constant current discharges. The noisy current load contains both discharge current and charge current, with a range between −0.4C (for charge) and 3C (for discharge). Fig. 5(c) shows the terminal voltage results. The model-predicted terminal voltage matches the measured value with an RMSE of 26.79 mV. The temperature results are shown in Fig. 5(d). The simulated temperature matches the experimentally measured temperature with RMSE of 0.20 °C for core temperature and RMSE of 0.20 °C for surface temperature.

4.1.4. Current switching

The rapid switching between charging and discharging modes for the cell is common during the practical use. Here the dECN model is validated in this extreme condition as an assessment of model capability. The cell SoC curve (blue dash-dotted curve) is W-shaped as shown in Fig. 5(e). The predicted terminal voltage results (orange dotted curve) against the experimental results (grey solid curve) are shown in Fig. 5 (e). The RMSE between the modelled voltage and measurement value is 39.12 mV. Fig. 5(f) shows the thermal model validation results. Again, the simulated core temperature (red dotted curve) and surface temperature (green dotted curve) match the measurement values (red solid curve for core temperature, green solid curve for surface temperature) well, with an RMSE of 0.58 °C and 0.74 °C for core and surface temperatures, respectively. The larger model error during charge is probably due to the fact that the electrical parameters in the ECN are obtained from discharge conditions.

4.2. Internal temperature estimation

In this section, the internal temperature for the LG M50T cylindrical cell was estimated by using the ECN model validated in Section 4.1, coupled with a Kalman filter algorithm. During the operation of the cell, the internal temperature of the cell core is usually unknown while the surface temperature can be monitored relatively easily. Through the Kalman filter, the temperature experimentally measured by the thermocouple placed on the cell surface mid-height is used as feedback to correct all internal temperature estimations, and in particular the core temperature. The core temperature measured by the inserted thermocouple is used to evaluate the accuracy of the temperature estimation.

Firstly, the internal temperature was estimated for passive conditions: zero current load and thus zero heat generation in the model. In the experiments, the instrumented cells with internal thermocouples were subjected to rapid temperature changes between 25 °C and 45 °C. The cells were submerged in a vat of thermally conductive, electrically insulating base oil (Etro 4+). The experiments were repeated twice. The measured core temperature is shown in Fig. 6(a–c) (solid black line). As shown in Fig. 6(a), the estimated core temperatures are successfully corrected to the experimentally measured values, for all initial guesses (0 °C, 10 °C and 30 °C). The ultimate core temperature estimation is independent of the initial temperature guess.

For cells within a battery system in a real application, measurement error of the surface thermocouple may be inevitable. The robustness of the temperature estimation method with respect to this error is evaluated by introducing random measurement noise, with normal distribution $N(\mu,\sigma^2)$. A disturbance noise error with mean $\mu = 0$°C and standard deviation $\sigma = 5$°C is added to the measured surface temperature as measurement input (light grey line in Fig. 6(b)). The estimated core temperature (grey dotted line in Fig. 6(b)) converges to the correct value (black solid curve in Fig. 6(b)). Another test of shift error (mean $\mu =$ 2°C, standard deviation $\sigma = 0$ °C) was performed, which also found the estimation is effective (Fig. 6(c)). The established estimation method is effective when the measurement error exists.

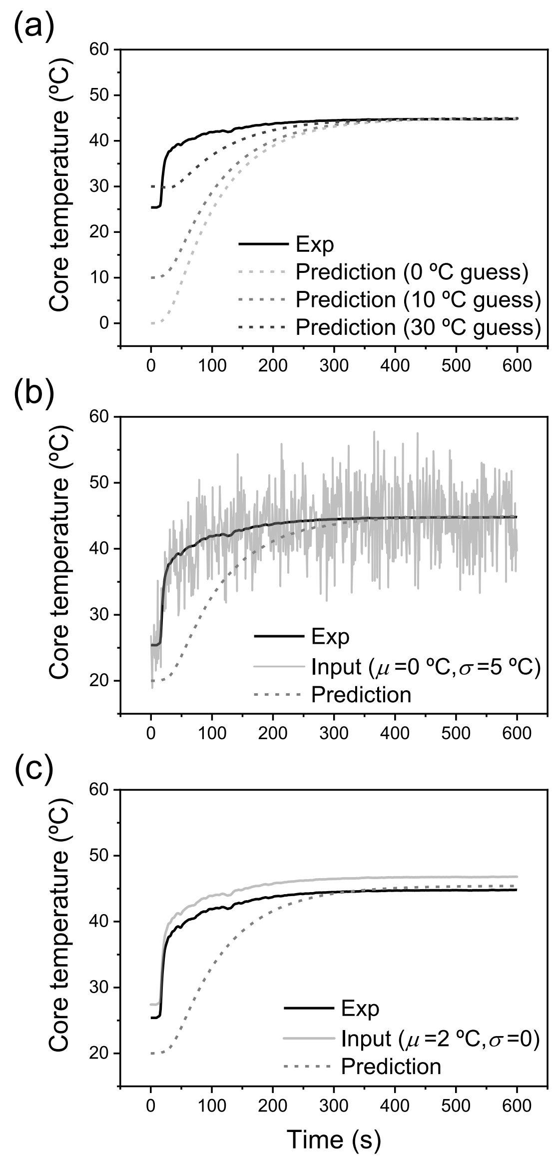

Fig. 6. Temperature estimation results for the check of robustness against errors of the input surface temperature measurement. (a) Estimation results for different initial guesses of the core temperature: 0 °C, 10 °C and 30 °C. Estimation results with measurement input noise error $N(\mu,\sigma)$: (b) disturbance error case with $\mu = 0$ °C, $\sigma = 5$ °C and (c) shift error case with $\mu = 2$ °C, $\sigma = 0$ °C. The core temperature measurement tests were repeated twice with RMSE of 0.15 °C. The experimental tests were repeated twice on two instrumented cells and the measurements are highly reproducible. For visual simplicity, only the first test result is shown.

Secondly, temperature estimation was performed under electrical loads. In the 1C (5 A) constant current discharge tests, the initial temperature guess was set as 0 °C. As seen in Fig. 7(a)–as discharge

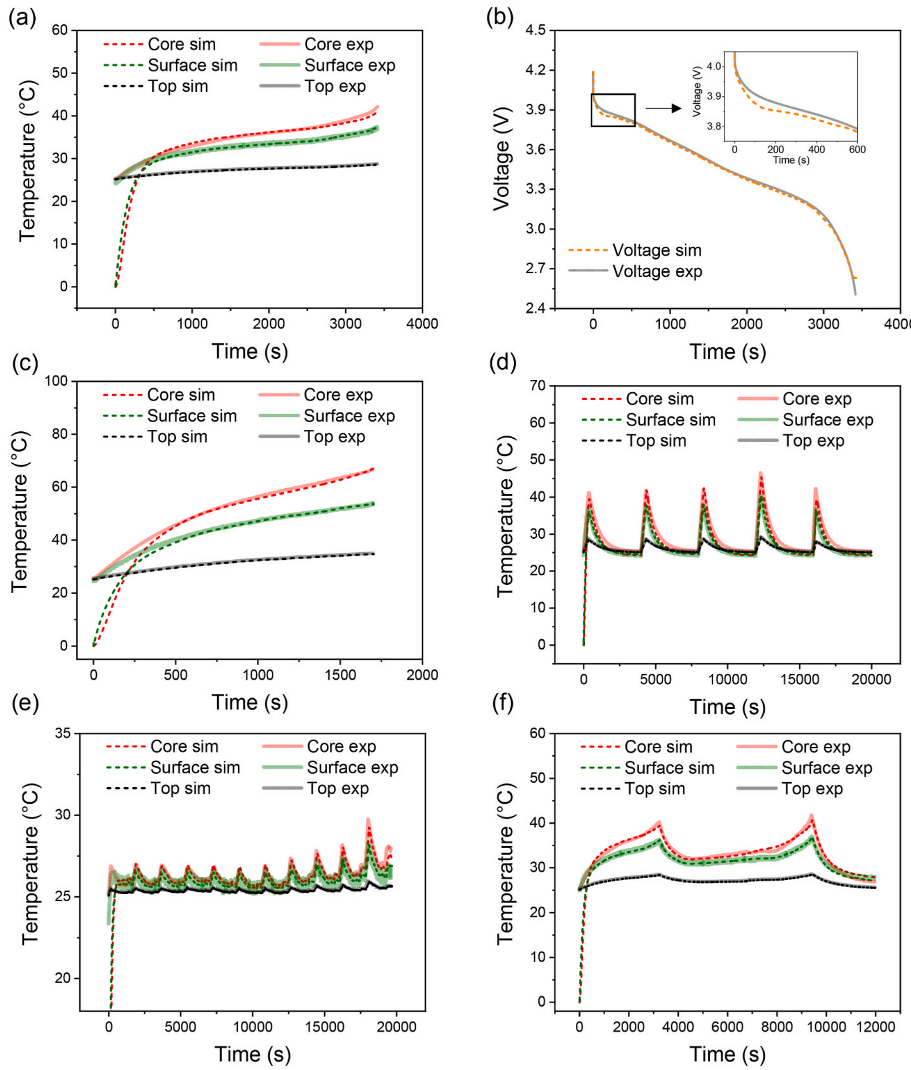

Fig. 7. Temperature estimation results for different current loads: (a) temperature and (b) terminal voltage for the 1C constant current discharge, with inset for the beginning of discharge. Temperature results for: (c) 2C constant current discharge, (d) pulse discharge, (e) drive cycle and (f) current-switching load. The experimental tests were repeated twice on two instrumented cells and the measurements are highly reproducible. For visual simplicity, only the first test result is shown.

progresses, the core temperature is corrected to the measured core temperature, respectively. After 600 s of discharge, the estimated core temperature tracks the experimental core temperature with an RMSE of 0.5 °C. Fig. 7(b) shows the model-predicted terminal voltage during the 1C discharge is close to the measured value. The inset in Fig. 7(b) shows the terminal voltage at the beginning of discharge, where there is a higher mismatch between the simulated and the measured values. This mismatch is the effect of the incorrect initial temperature guess of 0 °C, a much lower value than the real temperature, and leading to significantly higher internal resistances predicted in the model compared to in the experiment. The experimental data used here is the same as that used in Fig. 4(a, c).

Thirdly, the internal temperature was estimated under a wider variety of electrical loads: 2C (10 A) constant current discharge, pulse discharge, drive cycle and current-switching scenarios. The measured surface temperature and core temperature data for the internal temperature estimation are the same as displayed in Figs. 4(d) and Fig. 5(b, d and f) for those scenarios, respectively. The internal temperature estimation results are shown in Fig. 7(c–f). The initial temperature guess is set to 0 °C in all four load scenarios. The estimated core temperature converges to the measured core temperature, within the first 600 s of the estimation process. Therefore, the established thermal estimation model can perform hotspot detection with high precision under a wide range of electrical loads.

It is worth noting that the model validation and internal temperature estimation were performed based on model parametrization with beginning-of-life (BoL) experimental data. As a cell degrades, the dECN model would need to be updated to reflect the new states, such as increased resistance and decreased OCV capacity. While this is feasible, it falls out of the scope of this work.

4.3. Estimation from a two-node model

Two-node models [17,18] are frequently adopted for temperature estimation due to their low computational cost. However, the accuracy of these models cannot be guaranteed since those models are based on simple assumptions. In this section, the capability of the thermal estimation model proposed is compared with the two-node thermal estimation model [15] that is among the most advanced ones with electro-thermal coupling.

A two-node electro-thermal model of the LG M50T cylindrical cell is established by simplifying the dECN model along the radial direction. As shown in Fig. 8(a), in this simplified model there are only three nodes along the radial direction (one for the hollow core surrounded by separator, one for the electrode jellyroll and one for the metal can, respectively). For comparison, the fully discretized model validated in

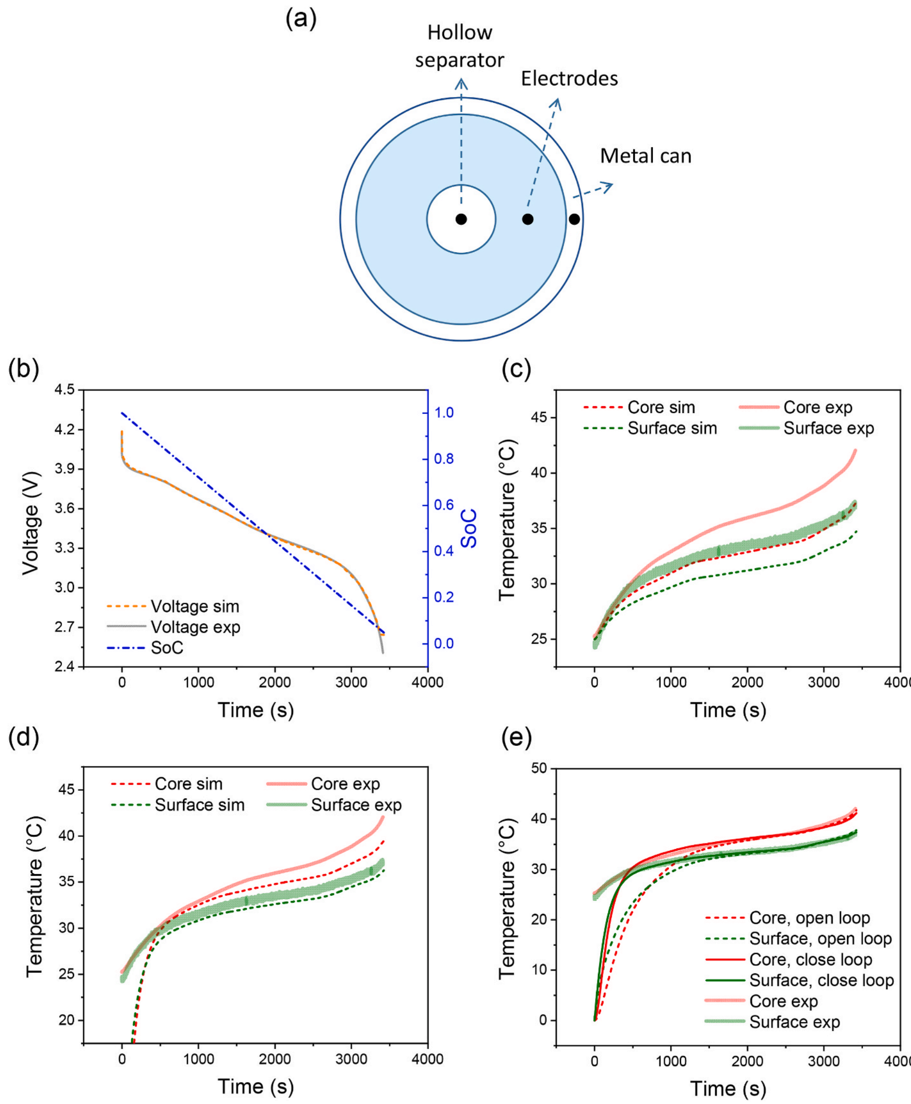

Fig. 8. Temperature estimation in simplified conditions: the two-node model and the fully discretized model in open loop. (a) Schematic representation of the two-node electro-thermal model. Validation results of the two-node model during a 1C (5 A) constant current discharge, for (b) terminal voltage and (c) temperature. (d) Temperature estimation results using the two-node model. (e) Temperature estimation results of fully discretized model in open loop mode.

Section 4.1 and used here in Section 4.3 includes 19 nodes along the radial direction.

Experimental voltage and temperature data from the 1C (5 A) constant current discharge (Fig. 4(a) and (c)) were used for validation of the two-node model. As shown in Fig. 8(b), the simulated terminal voltage is in good agreement with the experimentally measured voltage, with an RMSE of 10.09 mV. However, as shown in Fig. 8(c), the model-predicted temperatures deviate from the experimental temperatures significantly, with maximum errors at the end of discharge of 4.65 °C and 2.34 °C for the core and surface temperature, respectively. Using the same electrical and thermal parameters, it is clearly visible that the two-node model cannot capture the thermal behaviours in this 1C discharge test. The two-node model cannot capture the temperature inhomogeneity along the radial direction. Temperature estimation with the initial temperature guess of 0 °C was performed using the two-node model. As shown in Fig. 8(d), the core temperature estimation is unsuccessful - the estimated temperature does not converge to the experimentally measured value.

4.4. Open loop thermal estimation

In applications where battery packs are used, it is usually the case that only a limited number of cells, if any, have surface temperature sensing. The robustness and accuracy of the established temperature estimation model is studied for such cases in open loop, i.e., without surface temperature measurement input to the Kalman filter. The thermal estimation was performed in open loop for 1C constant current discharge test. The temperature results are shown in Fig. 8(e). The results of the 1C close loop thermal estimation are taken from Fig. 7(a). As shown in Fig. 8(e), the estimated core temperature performed in open loop can still converge to the experimentally measured value, albeit much slower than in the closed loop situation: roughly after 2000 s compared to 600 s. In applications where discharge, charge and relaxation mixed mode happen quickly, the internal temperature is expected to change significantly within a short time, such that the open loop estimation method may be inefficient for internal temperature estimation.

4.5. Application to industry

The internal temperature estimation tool established here is not restricted to the LG M50T cell used in this work, nor to a 21700 cell. It can be used, with adequate modification, for any lithium-ion battery, provided information on its structure and parametrization data is available. Indeed, the dECN model has already been developed and used to study the effects of cooling and internal structure of a 4680 tabless cylindrical cell [31], the inhomogeneous degradation of a pouch cell [32] and the cooling of a prismatic cell [33].

In order to test its capabilities on-line, the presented lightweight dECN model remains to be implemented into the TMS or BMS for real-time internal temperature estimation via the measured surface temperature. Apropriate testing of controller hardware and software should be performed regarding the system measurement requirement and safety operation issues. The dECN model should next be implemented into hardware-in-the-loop (HIL) simulator for the cost and time effective development of BMS. This is beyond the scope of the current work, and thus left for future development.

5. Conclusions

In this paper, a 3D distributed electro-thermal equivalent circuit network (dECN) model is developed for the temperature estimation on a cylindrical lithium-ion battery at its beginning of life. Compared with previous thermal estimation models, the model developed here exhibits higher accuracy even under aggressive discharge conditions and a relatively straightforward 3D electro-thermal framework, compared to a full electrochemical model. This allows the model to be used for a wide range of inhomogeneous thermal boundary conditions, with no limitation on their symmetry. The established model for core temperature estimation was validated against an instrumented LG M50T cell with direct monitoring of the core temperature. The model was validated under a wide range of discharge/charge scenarios including realistic drive cycles and extreme condition of constant current discharge at 2C, corresponding to the maximum C rate allowed from the specification sheet for this cell.

The established distributed model was compared to the widely used two-node lumped model, highlighting that the simplified model is unable of predicting cell internal temperature well, despite predicting the cell voltage with little error. The failure to take inhomogeneity into account therefore has a substantial impact on the temperature estimation accuracy. Without the surface temperature measurement as feedback, the core temperature estimation can still converge to the measured value in open loop mode under simple discharge condition. However, the estimation in close loop is significantly more efficient with surface measurement as feedback.

The model and results presented here should be of immediate interest to both cell manufacturers, module and pack designers.

CRediT authorship contribution statement

Shen Li: Conceptualization, Data curation, Formal analysis, Investigation, Methodology, Validation, Visualization, Writing – original draft, Writing – review & editing. **Anisha N. Patel:** Investigation, Writing – original draft. **Cheng Zhang:** Conceptualization, Validation, Writing – original draft. **Tazdin Amietszajew:** Investigation, Writing – original draft. **Niall Kirkaldy:** Data curation, Writing – original draft. **Gregory J. Offer:** Funding acquisition, Writing – original draft. **Monica Marinescu:** Funding acquisition, Methodology, Supervision, Writing – original draft, Writing – review & editing.

Declaration of competing interest

The authors declare that they have no known competing financial interests or personal relationships that could have appeared to influence the work reported in this paper.

Data availability

Data will be made available on request.

Acknowledgements

This work was generously supported by the EPSRC Faraday Institution Multi-Scale Modelling project (EP/S003053/1, grant number FIRG003, FIRG025 and FIRG059), the Innovate UK WIZer project (grant number 104427).

Appendix A. Supplementary data

Supplementary data to this article can be found online at https://doi.org/10.1016/j.jpowsour.2024.234701.

References

[1] Global EV Outlook 2020, 2020, https://doi.org/10.1787/d394399e-en.
[2] Y. Wang, X. Zhang, Z. Chen, Low temperature preheating techniques for Lithium-ion batteries: recent advances and future challenges, Appl. Energy 313 (2022) 118832, https://doi.org/10.1016/j.apenergy.2022.118832.
[3] L.H.J. Raijmakers, D.L. Danilov, R.A. Eichel, P.H.L. Notten, A review on various temperature-indication methods for Li-ion batteries, Appl. Energy 240 (2019) 918–945, https://doi.org/10.1016/j.apenergy.2019.02.078.
[4] H. Ruan, J. Jiang, B. Sun, X. Su, X. He, K. Zhao, An optimal internal-heating strategy for lithium-ion batteries at low temperature considering both heating time and lifetime reduction, Appl. Energy 256 (2019) 113797, https://doi.org/10.1016/j.apenergy.2019.113797.
[5] J. Zhu, M. Knapp, M.S.D. Darma, Q. Fang, X. Wang, H. Dai, X. Wei, H. Ehrenberg, An improved electro-thermal battery model complemented by current dependent parameters for vehicular low temperature application, Appl. Energy 248 (2019) 149–161, https://doi.org/10.1016/j.apenergy.2019.04.066.
[6] Z. Song, H. Hofmann, J. Li, J. Hou, X. Zhang, M. Ouyang, The optimization of a hybrid energy storage system at subzero temperatures: energy management strategy design and battery heating requirement analysis, Appl. Energy 159 (2015) 576–588, https://doi.org/10.1016/j.apenergy.2015.08.120.
[7] X. Feng, X. He, M. Ouyang, L. Lu, P. Wu, C. Kulp, S. Prasser, Thermal runaway propagation model for designing a safer battery pack with 25Ah LiNixCoyMnzO2 large format lithium ion battery, Appl. Energy 154 (2015) 74–91, https://doi.org/10.1016/j.apenergy.2015.04.118.
[8] X. Feng, J. Sun, M. Ouyang, F. Wang, X. He, L. Lu, H. Peng, Characterization of penetration induced thermal runaway propagation process within a large format lithium ion battery module, J. Power Sources 275 (2015) 261–273, https://doi.org/10.1016/j.jpowsour.2014.11.017.
[9] X. Feng, C. Weng, M. Ouyang, J. Sun, Online internal short circuit detection for a large format lithium ion battery, Appl. Energy 161 (2016) 168–180, https://doi.org/10.1016/j.apenergy.2015.10.019.
[10] I.A. Hunt, Y. Zhao, Y. Patel, J. Offer, Surface cooling causes accelerated degradation compared to tab cooling for lithium-ion pouch cells, J. Electrochem. Soc. 163 (2016) A1846–A1852, https://doi.org/10.1149/2.0361609jes.
[11] T. Waldmann, G. Bisle, B.-I. Hogg, S. Stumpp, M.A. Danzer, M. Kasper, P. Axmann, M. Wohlfahrt-Mehrens, Influence of cell design on temperatures and temperature gradients in lithium-ion cells: an in operando study, J. Electrochem. Soc. 162 (2015) A921–A927, https://doi.org/10.1149/2.0561506jes.
[12] R.R. Richardson, S. Zhao, D.A. Howey, On-board monitoring of 2-D spatially-resolved temperatures in cylindrical lithium-ion batteries: Part II. State estimation via impedance-based temperature sensing, J. Power Sources 327 (2016) 726–735, https://doi.org/10.1016/j.jpowsour.2016.06.104.
[13] J. Fleming, T. Amietszajew, J. Charmet, A.J. Roberts, D. Greenwood, R. Bhagat, The design and impact of in-situ and operando thermal sensing for smart energy storage, J. Energy Storage 22 (2019) 36–43, https://doi.org/10.1016/j.est.2019.01.026.
[14] K. Liu, K. Li, Q. Peng, Y. Guo, L. Zhang, Data-driven hybrid internal temperature estimation approach for battery thermal management, Complexity 2018 (2018), https://doi.org/10.1155/2018/9642892.
[15] C. Zhang, K. Li, J. Deng, Real-time estimation of battery internal temperature based on a simplified thermoelectric model, J. Power Sources 302 (2016) 146–154, https://doi.org/10.1016/j.jpowsour.2015.10.052.
[16] L. Sun, W. Sun, F. You, Core temperature modelling and monitoring of lithium-ion battery in the presence of sensor bias, Appl. Energy 271 (2020) 115243, https://doi.org/10.1016/j.apenergy.2020.115243.
[17] Y. Xiao, Model-based virtual thermal sensors for lithium-ion battery in EV applications, IEEE Trans. Ind. Electron. 62 (2015) 3112–3122, https://doi.org/10.1109/TIE.2014.2386793.
[18] H. Pang, L. Guo, L. Wu, J. Jin, F. Zhang, K. Liu, A novel extended Kalman filter-based battery internal and surface temperature estimation based on an improved electro-thermal model, J. Energy Storage 41 (2021) 102854, https://doi.org/10.1016/j.est.2021.102854.
[19] Y. Kim, S. Mohan, J.B. Siegel, A.G. Stefanopoulou, Y. Ding, The estimation of temperature distribution in cylindrical battery cells under unknown cooling conditions, IEEE Trans. Control Syst. Technol. 22 (2014) 2277–2286, https://doi.org/10.1109/TCST.2014.2309492.
[20] R.R. Richardson, D.A. Howey, Sensorless battery internal temperature estimation using a kalman filter with impedance measurement, IEEE Trans. Sustain. Energy 6 (2015) 1190–1199, https://doi.org/10.1109/TSTE.2015.2420375.

[21] A.M. Bizeray, S. Zhao, S.R. Duncan, D.A. Howey, Lithium-ion battery thermal-electrochemical model-based state estimation using orthogonal collocation and a modified extended Kalman filter, J. Power Sources 296 (2015) 400–412, https://doi.org/10.1016/j.jpowsour.2015.07.019.

[22] S. Li, N. Kirkaldy, C. Zhang, K. Gopalakrishnan, T. Amietszajew, L. Bravo Diaz, J. Varela Barreras, M. Shams, X. Hua, Y. Patel, G.J. Offer, M. Marinescu, Optimal cell tab design and cooling strategy for cylindrical lithium-ion batteries, J. Power Sources 492 (2021) 229594, https://doi.org/10.1016/j.jpowsour.2021.229594.

[23] Y. Zhao, Y. Patel, T. Zhang, G.J. Offer, Modeling the effects of thermal gradients induced by tab and surface cooling on lithium ion cell performance, J. Electrochem. Soc. 165 (2018) A3169–A3178, https://doi.org/10.1149/2.0901813jes.

[24] C. Veth, D. Dragicevic, R. Pfister, S. Arakkan, C. Merten, 3D electro-thermal model approach for the prediction of internal state values in large-format lithium ion cells and its validation, J. Electrochem. Soc. 161 (2014) A1943–A1952, https://doi.org/10.1149/2.1201412jes.

[25] D. Chen, J. Jiang, X. Li, Z. Wang, W. Zhang, Modeling of a pouch lithium ion battery using a distributed parameter equivalent circuit for internal non-uniformity analysis, Energies 9 (2016), https://doi.org/10.3390/en9110865.

[26] X. Hua, C. Heckel, N. Modrow, C. Zhang, A. Hales, J. Holloway, A. Jnawali, S. Li, Y. Yu, M. Loveridge, P. Shearing, Y. Patel, M. Marinescu, L. Tao, G. Offer, The prismatic surface cell cooling coefficient: a novel cell design optimisation tool & thermal parameterization method for a 3D discretised electro-thermal equivalent-circuit model, ETransportation 7 (2021) 100099, https://doi.org/10.1016/j.etran.2020.100099.

[27] T. Bergman, L. Adrienne, F. Incropera, D. DeWitt, Fundamentals of Heat and Mass Transfer, Wiley, n.d.

[28] A. Hales, L.B. Diaz, M.W. Marzook, Y. Patel, G. Offer, The Cell Cooling Coefficient : A Standard to Define Heat Rejection from Lithium-Ion Batteries, vol. 166, 2019, pp. 2383–2395, https://doi.org/10.1149/2.0191912jes.

[29] S.V. Erhard, P.J. Osswald, J. Wilhelm, A. Rheinfeld, S. Kosch, A. Jossen, Simulation and measurement of local potentials of modified commercial cylindrical cells, J. Electrochem. Soc. 162 (2015) A2707–A2719, https://doi.org/10.1149/2.0431514jes.

[30] K.J. Lee, K. Smith, A. Pesaran, G.H. Kim, Three dimensional thermal-, electrical-, and electrochemical-coupled model for cylindrical wound large format lithium-ion batteries, J. Power Sources 241 (2013) 20–32, https://doi.org/10.1016/j.jpowsour.2013.03.007.

[31] S. Li, M.W. Marzook, C. Zhang, G.J. Offer, M. Marinescu, How to enable large format 4680 cylindrical lithium-ion batteries, Appl. Energy 349 (2023) 121548, https://doi.org/10.1016/j.apenergy.2023.121548.

[32] M. Li, Zhang Shen, Zhao Cheng, Offer Yan, Marinescu Gregory, Effect of thermal gradients on inhomogeneous degradation in lithium-ion batteries, Nat. Commun. Eng (2023) 1–14, https://doi.org/10.1038/s44172-023-00124-w.

[33] S. Li, S.K. Rawat, T. Zhu, G.J. Offer, M. Marinescu, Python-based equivalent circuit network (PyECN) modelling framework for lithium-ion batteries: next generation open-source battery modelling framework for lithium-ion batteries. https://engrxiv.org/preprint/view/2972, 2023.

[34] R.E. Kalman, A new approach to linear filtering and prediction problems, J. Fluids Eng. Trans. ASME. 82 (1960) 35–45, https://doi.org/10.1115/1.3662552.

[35] J. Fleming, T. Amietszajew, A. Roberts, In-situ electronics and communications for intelligent energy storage, HardwareX 11 (2022) e00294, https://doi.org/10.1016/j.ohx.2022.e00294.

[36] J. Fleming, T. Amietszajew, E. McTurk, D. Greenwood, R. Bhagat, Development and evaluation of in-situ instrumentation for cylindrical Li-ion cells using fibre optic sensors, HardwareX 3 (2018) 100–109, https://doi.org/10.1016/j.ohx.2018.04.001.

[37] C. Zhang, Y. Guo, C. Wang, S. Li, O. Curnick, T. Amietszajew, R. Bhagat, A new design of experiment method for model parametrisation of lithium ion battery, J. Energy Storage 50 (2022) 104301, https://doi.org/10.1016/j.est.2022.104301.

[38] The Worldwide Harmonised Light Vehicle Test Procedure, No Title, (n.d.). https://www.vehicle-certification-agency.gov.uk/fuel-consumption-co2/the-worldwide-harmonised-light-vehicle-test-procedure/.